CrossMark

RESEARCH ARTICLE

Generation of vertical gusts in a transonic wind tunnel

V. Brion[1] · A. Lepage[2] · Y. Amosse[2] · D. Soulevant[1] · P. Senecat[1] · J. C. Abart[1]·
P. Paillart[1]

Abstract This article reports on the qualification of a gust generator device in a transonic wind tunnel. A vanning apparatus has been installed in the contraction of the S3Ch transonic wind tunnel at the ONERA Meudon center in order to generate up and down air movements in the test section. The apparatus has been tested in a range of Strouhal number based on frequency and vane chord up to 0.15 and in a range of Mach number between 0.3 and 0.73. The amplitude of the gusts has been characterized by a fast-response two-hole pressure probe and phase-averaged PIV. The system delivers vertical velocity amplitude of 0.5 % of the freestream velocity at transonic speeds. For a constant vane oscillation angle, the gust strength is found to increase with the Strouhal and the Mach numbers. The gust exhibit a satisfying uniformity and a quasi-sinusoidal waveform. A simple dynamic point vortex model of the oscillating vanes and of the downstream wake has been developed in order to (1) compare the experimental results and (2) enrich the description of the flow induced by the gusts. In particular, the model is used to analyze the detrimental effect of the upper and lower walls. This simple unsteady model gives a valuable prediction of the amplitude of the gust obtained in the tunnel and the workable frequency range permitted by the present apparatus.

✉ V. Brion
  vincent.brion@onera.fr

[1] The French Aerospace Lab, ONERA, Meudon, France

[2] The French Aerospace Lab, ONERA, Chatillon, France

1 Introduction

1.1 Background and motivation

Aerodynamic loads on an aircraft are subject to unpredictable variations due, for the most part, to turbulent disturbances induced by atmospheric flows. Among the main phenomena, one may mention natural instabilities of air masses, water–land discontinuities, thunderstorms and the effects of mountain terrain Clementson (1950). Those impact all phases of flight. Close to the ground, significant turbulence levels can be encountered due to the flow variations associated with the atmospheric boundary layer, particularly in case of intense radiative forcing. At high altitudes, vertical velocity up to 10 m/s and sustained velocities of 3–5 m/s have been reported inside a cumulus cloud by Levine et al. (1973). It seems, however, that such harsh conditions of flight have caused only few accidents in the past (Krause 2003). On a less extreme basis, low-to-medium unsteady aerodynamics loads can lead to passenger injuries, discomfort or deterioration of goods. Requirements that apply on an aircraft submitted to gust-induced loads are described in the CS-25 and FAR-23/25 certification documents (European Aviation Safety Agency 2013), applicable to medium and large transport aircrafts. The severity of a gust is estimated in terms of Δn which is the increase in load factor expressed in units of gravity acceleration g (in m/s^2). It must not exceed 2.5 g at the pilot's seat (Reginald et al. 1947). Such limits are reserves for unexpected events, for instance avoidance maneuvers. In this context, predicting the way an aircraft behaves under aerodynamics loads, and eventually reducing the sensibility to them, is of high importance. Numerical simulations are useful to do so (Liauzun 2010; Huvelin et al. 2013). The development of improved aeroelastic models requires

extensive experimental database, which are currently lacking, especially in the transonic regime.

The work described in the present article is the preliminary part of a large experimental program, accomplished within the Clean-Sky European project, whose first objective is to build such an experimental database. In this context, the response of a wing model to vertical gusts will be investigated using a 2D supercritical airfoil and the well known two degrees of freedom aeroelastic model (pitch and plunge motion). The second objective is to demonstrate the capacity to alleviate the gust loads through the active control of the aeroelastic response of the wing model, by using a remote control surface in a closed-loop approach.

In the present work, the objective is to qualify the gust generator device on its own. The experiment is carried out in the S3Ch transonic wind tunnel at ONERA. The apparatus consists in a tandem of oscillating airfoils installed horizontally right upstream of the test section, at the end of the nozzle. The generator is set so as to deliver deterministic vertical and harmonic gusts in a flow dynamically scaled in Mach number. Mach between 0.3 and 0.73 have been tested. The objective of these tests is to qualify the gusts in the empty test section, in terms of amplitude, spatial and temporal form. Measurements are performed in a volume centered about the middle of the test section in the longitudinal (freestream) direction. Two measurement devices have been used: a time-resolved two-hole pressure probe that allows to quantify the flow angle at a selection of locations and a phase-averaged planar PIV system applied in a vertical plane aligned with the freestream. A dynamic model of the flow has also been numerically implemented to complement the experimental analysis. In particular, the dynamic model provides information in the entire flow field while the measurements are limited in space. It also provides the effect of the gust frequency on a wider range than that accomplished in the experiment and help quantify the effect of the test section upper and lower walls on the gust amplitude.

Previous works in the field of experimental gust generation show a great diversity of techniques. For instance, free flight experiments have been used by Kobayakawa and Maeda (1978). In Kobayakawa's setting the aircraft is propulsed into the air, and a jet is produced at some point of the free flight to mimic the gust. Apart from this free flight experiment, most studies concern gust generation in wind tunnels. The basic idea for generating gusts in a closed channel is to modify the boundary conditions in an unsteady manner, either at the inlet, at the walls of the channel, or at the surface of the model. Moving the model or the walls with a possibly high frequency is a difficult task which does not seem to have ever been attempted. One exception concerns the wind tunnel tests that used two rotative square cylinders installed at the surface of the

upper and lower walls of the nozzle of the S3Ch wind tunnel at ONERA which is also used in the present work (see Brunele and Consigny 1989). Yet this technique showed poor performances and induced strong vibrations upon the wind tunnel walls. The modification of the inlet flow seems to be the prevailing technique. This is what the present arrangement does. The two vane devices that are used is in fact very close to that installed by Ricci and Scotti (2008). A vane arrangement was also used by Buell (1969) with a larger number of vanes and a span smaller than that of the wind tunnel, at low speed. By playing on the phase between the vanes, Buell could generate either horizontal or vertical gusts. Grissom and Devenport (2004) used a similar system with multiple vanes in the contraction of a wind tunnel at low speed. Mirick et al. (1990) implemented a double pair of oscillating stumps installed at the side walls of the contraction of the Langley transonic dynamics wind tunnel. Unlike full-span arrangements, the gust generated by the stumps are induced by the longitudinal vortices shed at the stump tips. Reid and Wrestler (1961) later used this apparatus up to Mach 0.8 to investigate the response of a delta wing to gusts. Bennett and Gilman (1966) investigated the response of a flexible fighter set in free flight condition with an oscillating airfoils apparatus in the Langley transonic wind tunnel. Mai et al. (1961) performed tests in the transonic wind tunnel of the DLR Gottingen center with a single pitching airfoil and a three-dimensional flexible wing in the test section. Tang et al. (1996) used a pair of slotted cylinders located downstream of airfoils and, by spinning the cylinders, he could provide varying flow orientation, thus causing gusts. It is to be noted that tests at high speeds are rare. This can be explained by the fact that when the flow speed increases, the frequency range of interest also increases, making traditional oscillating devices relatively too slow. Borland and Schindel (1967) bypassed that problem by using pulsating jets, which have less limitation than mechanical systems, to perform tests at supersonic flow speeds.

The major objective of gust generation in a closed channel is the production of uniform gusts with the desired waveform and amplitude. In the present mechanism, the gust is produced by the wake vorticity of the two airfoils, which basically transports the down and up washes generated by the moving airfoils behind them. In this situation, the main obstacles to the gust amplitude, waveform and uniformity are the interferences produced by the wake vortices and by the channel walls. Namely, the wakes limit the zone of uniform and low turbulent flow in the test section. When using two airfoils, the clean part of the flow is that in between the airfoils. The problem of a single wing setting, such as the one used by Mai et al. (1961), is that the part of the channel downstream of the airfoil, where typically a flexible is installed, suffers from wake interferences. In

Mai's study, the model is placed in the wake of the oscillating airfoil, which leads to additional turbulent forcing upon the model. The effect of the channel walls depends upon the ratio between the streamwise wavelength of the gust and the channel transverse dimension. For a given frequency of oscillation, higher flow speeds are more prone to be affected by the walls because they produce longer wavelengths and, in turn, more intense potential flow variations in the farfield. As mentioned earlier, only few tests have been performed at transonic speeds (Reid and Wrestler 1961; Mai et al. 1961). High velocities also make the aerodynamic loads on the oscillating airfoils more intense, making challenging the actuation of the oscillating vanes. These loads increase as M^2 since the pitching moment on the airfoil is

$$T = \frac{1}{2} p_0 \gamma \left(1 + \frac{\gamma - 1}{2} M^2 \right)^{\frac{-\gamma}{\gamma - 1}} M^2 C_M S$$

where p_0 is the stagnation pressure, γ the perfect gas constant, C_M the pitching moment coefficient and S the wing planform area. Oscillating the airfoil at higher Mach numbers thus requires powerful actuators.

The organization of the paper is as follows. First, in the following subsection, the basic ingredients of the gust generation process are presented, using a simple analytical model. In Sect. 2, the full experimental assembly including the wind tunnel, the gust generating device and the measurement tools is described. Preliminary experimental data are presented, which validates the harmonic waveform of the gusts. Sect. 3 presents the dynamic model corresponding to the experimental setup. Sect. 4 describes the experimental data. An analysis of the gust amplitude, uniformity and harmonic shape are carried out and comparisons against the dynamic model are performed. In the end, the dynamic model is further used to quantify the working range of the generator device.

1.2 A basic view of the gust generation process

To introduce the concept of gust generation, a simple gust generator device, constructed with one oscillating airfoil, such as the one used by Mai et al. (1961), is first considered. A potential flow model of the setup is derived and used as an introductory material to discuss the essential parameters of the system. An incompressible model is first built and the effect of compressibility is then introduced with the Prandtl-Glauert analogy.

Figure 1 illustrates this simple setting. It shows the oscillating airfoil in a uniform channel flow of velocity U_0. The channel height is H and the width is W. The objective is to generate vertical gusts in the region $x \simeq l$ downstream of the airfoil. The oscillating wing is chosen with
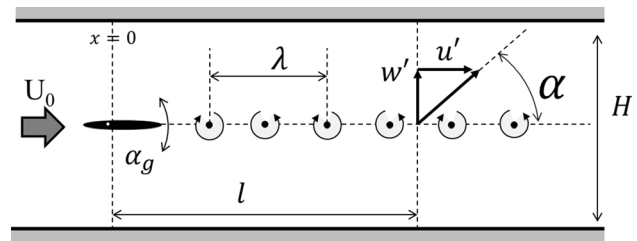

Fig. 1 Simple schematic of the gust generator

a high aspect ratio, thus reducing the problem to a 2D setting and neglecting the effect of the width W. Considering a harmonic motion, the pitch angle of the airfoil evolves following

$$\alpha_g = A_g \cos \left(2\pi f_g \right) \tag{1}$$

where f_g is the frequency and maximum pitch angle is A_g. The amplitude A_g is kept small enough to avoid nonlinear effects. The wake of the airfoil is formed of aligned discrete vortices such that a wake vortex is released at every reversal of the airfoil motion, when the bound circulation Γ_g changes sign. Introducing the normalized frequency St (Strouhal) based on the frequency f_g, wing chord c and free stream velocity U_0, it can be shown that the vortex distribution forms an array of period $\lambda = c St^{-1}$. The vortices have strengths $\pm \Gamma_v$, where Γ_v is set positive. The vortex strength directly results from the lift L produced by the incoming flow upon the airfoil. According to the Joukowsky law $L = \rho_0 U_0 \Gamma_g$ where ρ_0 is the mass density in the free stream. The straight wake line is a simplification that allows analytical derivation. It is a priori valid in the near field behind the airfoil where the wake suffers only small deformations. The flow downstream of the airfoil is modified by the horizontal and vertical velocity components u' and w'. The flow incidence evolves as $\alpha = A \cos \left(2\pi f_g + \phi \right)$ where $A = \frac{w'}{U_0}$ is the maximum angle of the gust and $\phi = \frac{l}{2\pi U_0}$ is the phase delay corresponding to the transport of the gust from the pitching airfoil to the measurement location at $x = l$. This delay is based on the hypothesis that the gust is transported at the speed U_0. Using the phase signal obtained with the two-hole pressure probe in the present experiments, this was found to be a good approximation. In fact a growing difference is observed as the Mach is increased, but even for the highest Mach number investigated here ($M = 0.73$), the difference can be reasonably neglected.

The previous system can be made dynamically consistent, while keeping a straight vortex line, by applying the correction due to the wake forces that, in fact, act upon the airfoil. Theodorsen (1992) obtained a closed-form solution to the problem of the unsteady aerodynamic loads on an oscillating aerofoil. Theodorsen's approach makes the assumptions of sinusoidal oscillations of small amplitude
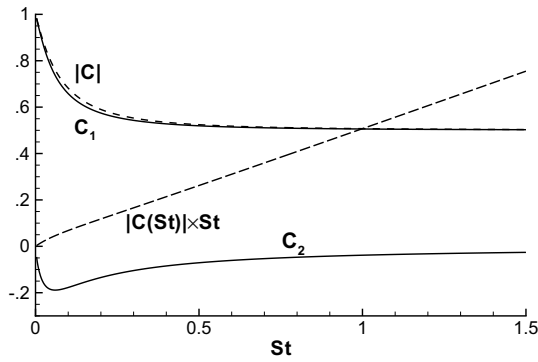
Fig. 2 Evolution of the Theodorsen lift-deficiency function as a function of the Strouhal number St. The *plot* shows the real and imaginary parts C_1 and C_2, the magnitude $|C|$ of the function $C(St)$, and the product $|C(St)| \times St$ that appears in relation (7)

in an inviscid and incompressible flow, like in the present case. It provides a correction to the static lift which is called the lift-deficiency function C given by

$$C(St) = \frac{-J_1(St) + iY_1(St)}{-(J_1(St) + Y_0(St)) + i(Y_1(St) - J_0(St))} \quad (2)$$

where the J's and Y's are Bessel functions. The real and imaginary parts of C are noted C_1 and C_2, respectively. In the limit of small Strouhal numbers, i.e., quasi-steady motion, $C \to 0$ and the lift is given by the Joukowsky law. For a finite Strouhal number, the lift needs to be corrected with the amplitude of C. In the following, we thus consider the corrected lift $|C(St)|L$. The evolution of the function C as a function of the Strouhal number is shown in Fig. 2. It is remarkable that the dynamic correction rapidly reaches a significant magnitude, even in the low Strouhal range.

Considering the above purely sinusoidal setting, the main quantity of interest is the gust maximum angle A, which, on general grounds, can be written as

$$A = f\left(St, A_g, M, \frac{H}{c}\right) \quad (3)$$

The influence of l has been neglected owing to the assumption that the wake is transported without change and that the flow is observed close behind the airfoil. The Mach number is accounted for using the Prandtl-Glauert analogy. The function f is obtained by relating the strength Γ_v of the wake vortices to the airfoil varying lift. This is first achieved by considering the flow without the upper and lower walls (i.e., $H \to \infty$). Differentiating the Joukowsky law yields $\Delta L = \rho_0 U_0 \Delta \Gamma_g$. Then, invoking the lift characteristic of the airfoil $C_L(\alpha_g)$, one also has

$$\Delta L = \frac{1}{2}\rho_0 U_0^2 \frac{dC_{L0}}{d\alpha} \Delta \alpha_g \quad (4)$$

A vortex is shed at every reversal of the pitch motion, when $\Delta \alpha_g = 2A_g$, and, since $\Gamma_v = |C(St)|\Delta \Gamma_g$, combining the previous relations gives

$$\Gamma_v = \frac{dC_{L0}}{d\alpha} U_0 A_g c |C(St)| \quad (5)$$

Using a point vortex model, the vortex-induced tangential flow writes $u_\theta = \frac{\Gamma_v}{2\pi r}$ where r is the radius about the vortex center. The maximum vertical perturbation velocity is obtained at $r = \lambda/4$, halfway between two vortices. The vertical velocity induced by these two vortices is equal to $w' = 4\frac{\Gamma_v}{\pi \lambda}$, which yields the following amplitude of gust

$$\frac{A}{A_g} = \frac{4}{\pi} \frac{dC_{L0}}{d\alpha} |C(St)| St \quad (6)$$

This relation is important as it shows that the gust amplitude linearly depends on the pitch angle of the airfoils and evolves with the Strouhal number in a way that is determined by a linear law modulated by the Theodorsen's correction.

At last, the Prandtl-Glauert transformation allows to model the effect of compressibility. According to this approach $C_L = \beta C_{L0}$ with $\beta = \frac{1}{(1-M^2)^{1/2}}$ where C_{L0} is the value of the lift coefficient in the incompressible limit introduced above. Further considering $\frac{dC_{L0}}{d\alpha} = 2\pi$ which is valid for a thin and symmetrical airfoil at small angle of attack, then (6) yields

$$\frac{A}{\beta A_g} = 8|C(St)| St \quad (7)$$

This relation shows the beneficial effect of the Mach number on the gust amplitude, which is directly associated with the improved airfoil performance. Importantly it demonstrates that the Strouhal number and the pitch angle A_g are the dominant parameters of the flow.

This model is valid in the absence of walls. The effect of H can be assessed by the additional use of image vorticity. The system of image vortices for each vortex of Fig. 1 comprises two infinite arrays of opposite sign vorticity with a wavelength $2H$ in the vertical direction. The velocity induced by an infinite array of point vortices in the vertical direction with period $a = 2H$ is given by Lamb (1993).

$$u_{a,x_0,z_0}(x,z) = -\frac{\Gamma_v}{2a} \frac{\sin\left[\frac{2\pi}{a}(z-z_0)\right]}{\cosh\left[\frac{2\pi}{a}(x-x_0)\right] - \cos\left[\frac{2\pi}{a}(z-z_0)\right]}$$

$$w_{a,x_0,z_0}(x,z) = \frac{\Gamma_v}{2a} \frac{\sinh\left[\frac{2\pi}{a}(x-x_0)\right]}{\cosh\left[\frac{2\pi}{a}(x-x_0)\right] - \cos\left[\frac{2\pi}{a}(z-z_0)\right]}$$

$$(8)$$
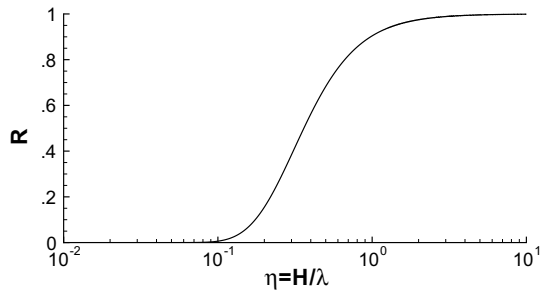
Fig. 3 Evolution of the ratio R of the vertical velocity induced with and without the upper and lower walls, as defined in (9), as a function of $\eta = H/\lambda$

Fig. 4 Evolution of the incidence ratio $A/\left(\beta A_g\right)$ as a function of the Strouhal number for the analytical models (7) and (10) without and with the walls, respectively

where (x_0, z_0) is the position of the vortex at the center of the array. The first array is based on the vortex located at $z_1 = 0$ and x_1, x_1 spanning the wake. The second array is based on the image vortex located at $z_2 = -H$ and $x_2 = x_1$. It is straightforward to verify that in the limit $H \to \infty$, the velocity field amounts to that of a single point vortex (u_0, w_0). To evaluate the influence of the height H on the gust amplitude, the ratio

$$R = \frac{\left(w_{a=2H,0,0} + w_{a=2H,0,-H}\right)}{w_0}$$

is calculated on the (Ox) axis at the location in between two vortices (i.e., at $\lambda/4$ where the maximum vertically induced velocity occurs. Taking equation (8) then yields
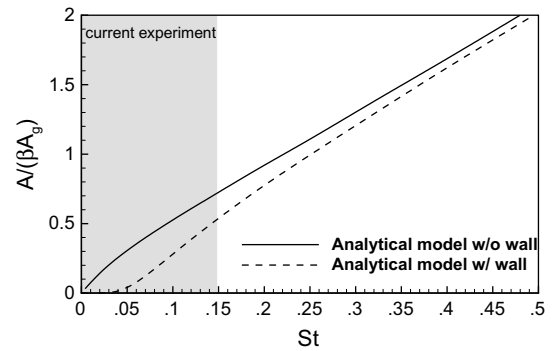
$$R(\eta) = \frac{\pi}{4\eta} \frac{1}{\sinh\left(\frac{\pi}{4\eta}\right)} \tag{9}$$

where $\eta = H/\lambda$ is the ratio of the channel height to the gust wavelength. Note also that $\eta = StH/c$. The curve $R(\eta)$ is shown in Fig. 3. It shows that the influence of the wall is reduced for small wavelengths whereas large wavelengths are significantly impacted. This traduces the influence of the image vortices. In the short wavelength case, the gust amplitude is less influenced by the image vortices because the wake vortices are relatively close to each other. As the wavelength is increased, i.e., η decreases, the influence of the image vortices becomes strong and ends up being dominant. When the walls are present, relation (7) must be corrected using this ratio R as follows

$$\frac{A}{\beta A_g} = 8|C(St)|St\tilde{R}(St) \tag{10}$$

where $\tilde{R}(St) = R(\frac{H}{c}St)$.

Figure 4 shows the evolution of the incidence ratio $A/\left(\beta A_g\right)$ as a function of the Strouhal number using relation (10), for the cases with (H finite) and without the walls ($H \to \infty$). These results indicate the positive effect of the Strouhal number on the gust amplitude and the negative

effect of the walls, especially when St is small (i.e., long wavelengths). For instance the gust amplitude is almost halved at $St = 0.1$. For higher frequencies, say $St > 0.25$, this reduction decreases below 10 %. The Strouhal range of the current wind tunnel test is marked by the gray area. It shows that the gust amplitude in the present case is strongly deteriorated by the walls.

## 2 Description of the experimental setup

2.1 Wind tunnel

The S3Ch WT is a transonic facility that generates flow velocities from Mach 0.3 to 1.2. It is a closed-circuit wind tunnel operated at atmospheric stagnation pressure and stagnation temperature of approximately 310 K. The air is entrained by a two-stage fan powered by a 3.5 MW engine. The power is adjusted by pitching the fan blades, the rotational speed being constant. The test section is rectangular with a height of 0.76 m, a width of 0.804 m and a length of 2.2 m. It is equipped with adaptive upper and lower walls in order to create infinite flow field test conditions. In the present experiment, the test section is empty and the walls are set flat with a slight divergence to account for the boundary layer growth and maintain a constant Mach number in the test section. The coordinate system attached to the test section is as follows: the (Ox) axis points downstream in the direction of the flow, the (Oy) axis is horizontal oriented to the right when one is face to face with the flow, and the (Oz) axis is vertical pointing upward.
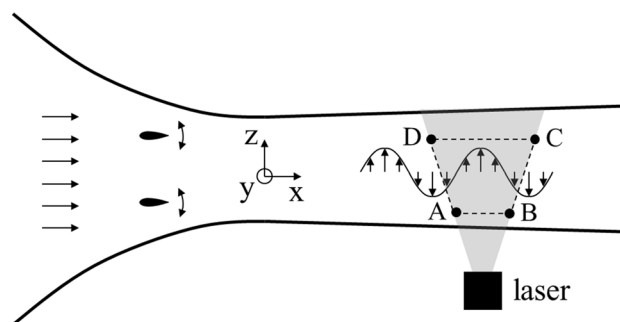
2.2 Gust generator device

The gust generator has been designed at ONERA in the department of aeroelasticity. Figure 5 shows the apparatus inside the wind tunnel, as it would be seen when one
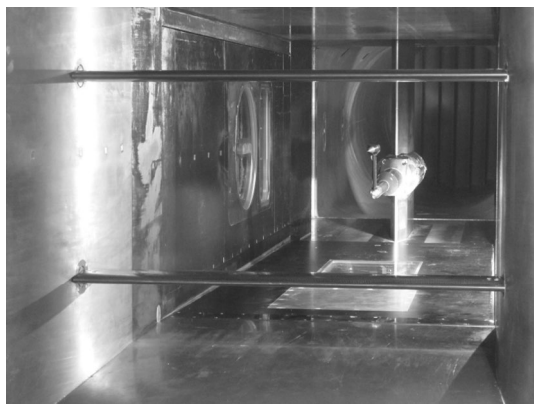
Fig. 5 Picture of the gust generator. The view is from *upstream*. The two-hole pressure probe, held from a *downstream* holder, is visible in the *back*

Fig. 6 Schematic of the apparatus. The oscillating airfoils are positioned in the nozzle. *Up* and *down* velocities are generated in the test section whose walls are slightly diverging to account for the growth of the boundary layer and maintain a constant Mach over the length of the test section. The laser is installed below the test section such as illuminating a vertical *plane* aligned with the flow. The PIV *plane* is the volume *ABCD*

is placed upstream of the test section. The gust generator is made of two identical NACA0012 airfoils of $c = 0.2$ m chord length placed at $x_w = 0.63$ m, upstream of the entrance of the test section which corresponds to $x = 0$, and at $h_g = 0.2$ m above and below the wind tunnel longitudinal axis. The longitudinal location of the airfoils corresponds to the nozzle part of the wind tunnel. Although the NACA0012 profile is known to separate early, the fact that the angle of attack is kept small prevents any unwanted separation. As seen in Fig. 5, the airfoils span the entire width of the tunnel. They are made of an optimized architecture that combines composite and metallic parts to reduce inertia and allow high frequencies of actuation under heavy aerodynamic loads. In addition to inertial and strength constraints, the dynamic behavior of the airfoils was tuned such that the frequency of the first flexible structural mode is higher than the frequency bandwidth of the gust generator, i.e., 100 Hz. Preliminary to the wind tunnel tests, the complete experimental setup was qualified under laboratory conditions to identify the static and dynamic behaviors of each airfoil and to verify the performances of the actuation in pitch. In particular, dynamic tests results were used in an aeroelastic calculation procedure to ensure the absence of any instability (flutter, static divergence) in the range of the wind tunnel test conditions. The airfoils are equipped with accelerometers, pressure transducers and deformation gauges. In particular, one of the deformation gauge is used to deliver an approximate measure of the variations of the aerodynamic loads. The actuation is performed by four servohydraulic jacks which synchronously rotate the two airfoils. Each airfoil is driven at its two sides and the actuation device includes a security system that stops the actuation whenever the two roots of one airfoil are not at the same angular position, thus preventing any unwanted torsional deformation of the airfoils. The airfoils pitch about the quarter chord point

at frequencies up to 80 Hz in air streams up to Mach 0.73 for atmospheric stagnation conditions. An additional degree of freedom is the adjustable incidence, at rest, of each airfoil. It is used to adapt the airfoil incidence to the local flow angle generated at the end of the nozzle where the oscillating airfoils are placed. The airfoils are supported outside the wind tunnel to prevent the presence of struts in the flow like in the study of Grissom and Devenport ([2004](#)). The wing tips are in the shape of the contraction part of the wind tunnel so that there is a minimal and approximately constant gap (of the order of 1mm) between the wing tip and the wind tunnel walls (Fig. 6).

The parameter space is described in Table 1. The experimental tests are characterized by the upstream Mach number, the pitch frequency f_g and amplitude A_g. Considering inertial loads on mechanical components and hydraulic flow rate, the achievable oscillation amplitude A_g is reduced when the frequency or the Mach increases, which explains the variations in the parameter sets. Moreover, although different dynamic laws can be applied to the oscillating airfoils, such as harmonic, step and sweep, only the harmonic case is treated in the present work. The flow in these sets of parameters have been qualified using the fast-response two-hole pressure probe and the PIV, as described in the following section.

Table 1 Set of parameters investigated in the experiment. The PIV test cases have been numbered from 1 to 6

f_g (Hz)	$M = 0.3$	$M = 0.5$	$M = 0.6$	$M = 0.73$
20	5° (PIV 1)	5°	5°	3° (PIV 4)
40	2° (PIV 2)	2°	2°	2° (PIV 5)
60	1°	1°	1°	1°
80	0.5° (PIV 3)	0.5°	0.5°	0.5° (PIV 6)

Fig. 7 Sketch of the two-hole pressure probe. The front diedral makes an angle of 90°. The two pressure sensors are inserted inside the core of the probe

2.3 Measurement devices

2.3.1 Fast-response two-hole pressure probe

A time-resolved two-hole pressure probe has been used to characterize the flow incidence in time and space. The probe is sketched in Fig. 7. It features a $\phi_p = 5$ mm diameter nose with a 90° diedral front. Two unsteady pressure sensors are located inside the tube and directly fed to the exterior through channels 0.4 mm in diameter. The probe is held from a downstream support, which can be seen in Fig. 5, allowing to scan the test section in a pointwise manner.

The probe was first calibrated in order to determine the relation between the pressure difference $\Delta p = p_2 - p_1$ between the two sensors, with p_1 and p_2 referring to the upper and lower sensors, respectively, and the flow incidence α. The calibration was performed in the test section of the S3Ch wind tunnel, without the gust generator. To do that, the pitch of the probe holder was varied in order to generate prescribed flow angles for a steady incoming flow. Since the rotation center of the probe holder is not located at the head of the probe, the vertical position of the ensemble made by the probe and the holder had to be adjusted in order to keep the position of the head of the probe fixed. The calibration was also performed with the probe set upside down in order to differentiate the probe defects and the natural flow incidence in the test section.

This step provided the static calibration of the probe. The probe was then used for a dynamic assessment of the flow angle. The validity of the static calibration for dynamic measurement is guaranteed by the extremely low Strouhal number of the gust induced flow variations investigated in the present work, when scaling is done on the probe diameter ϕ_p. Introducing $St_p = \frac{f_g \phi_p}{U_0}$ such a Strouhal number, and considering, in this respect, the most challenging parameters set $f_g = 80$ Hz and $U_0 \simeq 100$ m/s when $M = 0.3$, yields $St_p = 4 \times 10^{-3}$, an indeed small value. The flow, when dynamically scaled to the probe parameters, is almost steady, hence fully validating the use of the static calibration for the temporal description of the gust signal.

Figure 8 shows the steady probe response as a function of the flow incidence for various Mach numbers. The
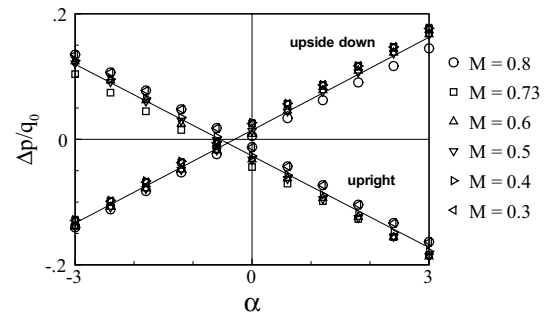
**Fig. 8** Calibration curve of the two-hole pressure probe in the *upright* and *upside down* positions

pressure difference is normalized against the upstream dynamic pressure $q_0 = \frac{1}{2}\rho U_0^2$ where ρ is the density inside the channel, related to ρ_0, the stagnation mass density, through $\rho = \rho_0 \left(1 + \frac{\gamma - 1}{2} M^2\right)^{\frac{-1}{\gamma - 1}}$. The response in the upside down position of the probe delivers an opposite pressure difference. A small dispersion of the data in terms of Mach number is observed. The pressure difference does not cancel with α, which traduces the natural flow incidence in the center of the test section. The average probe calibration over the ensemble of Mach numbers is found to be $\alpha = 20\frac{\Delta p}{q_0}$, with a small dispersion in Mach number. In the post-processing of the probe data, a Mach-dependent calibration was used.

The probe was used to measure the changes in the flow angle. The vibrations of the probe had to be avoided in certain situations, because they induced apparent variations in the measurement. In these cases, additional cables were installed between the wind tunnel walls and the probe so that it was kept fixed.

Typical temporal signals obtained by the probe when the gusts are generated are shown in Fig. 9, along with the associated spectrum charts. The probe is placed at the position at $x = 1.1$ m on the longitudinal axis. The data show that the gust generator delivers close to pure harmonic waveforms. The raw signals suffer only low noise, and only a small disturbance modulation of the signal is observed. The spectral analysis exhibits a principal component at the airfoil oscillation frequency and several higher-order harmonic with a much lower magnitude. In this situation, the amplitude of the gust is easily obtained by taking the intensity of the peak of the principal component.

2.3.2 Particle image velocimetry

Two-component phase-averaged Particle image velocimetry (PIV) is also used to qualify the flow. The PIV setup is made of a double-pulse Litron laser of 200 mJ energy,
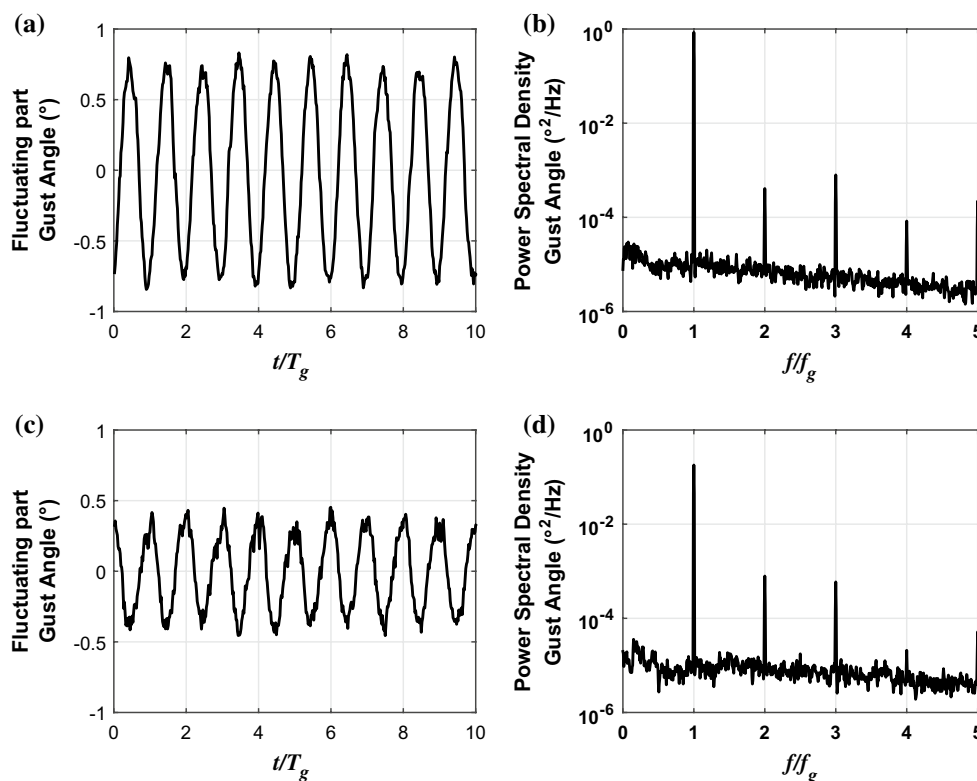
Fig. 9 Signals obtained by the two-holes pressure probe and the associated spectra. **a, b** $M = 0.3$ and $f_g = 40$ Hz. **c, d** $M = 0.73$ and $f_g = 40$ Hz

working at 2 Hz and a 12 bits resolved camera with 11 M pixels spatial resolution (4000 × 2672 pixels), one pixel being a square of size 7.4 µm. A 50-mm lens is used which gives a physical dimension in the measurement plane of about 0.15 mm per pixel. The laser is installed below the test section and delivers an (Oxz) laser sheet at a prescribed position in along the (Oy) direction, as schematized in Fig. 6. Two transverse positions were investigated, $y = 0$ and $y = 130$ mm. The laser source being rather close to the bottom of the test section, a significantly diverging laser sheet is produced so as to enlarge the measurement plane. The measurement plane features a trapezoidal shape with the four corners indicated in Fig. 6 at $A(1 \, \text{m}, -0.25 \, \text{m})$, $B(1.45 \, \text{m}, -0.25 \, \text{m})$, $C(1.5 \, \text{m}, 0.25 \, \text{m})$ and $A(0.9 \, \text{m}, 0.25 \, \text{m})$. The top and bottom of the PIV domain are 0.15 m away from the walls. The airfoils wakes appear at approximately ±0.2 m. All the PIV recordings, along with the flow parameters, are listed in Table 1. The PIV cases 1, 2, 3, 5, 6 and 7 were obtained at the transverse location $y = 0$ while PIV cases 4 and 8 were obtained at $y = 13$ mm. Due to the higher complexity of the PIV measurements, fewer test points than with the pressure probe were recorded.

The seeding particles are DEHS particles of micrometric size generated by an in-house system composed of several Laksin nozzles which pulverize the liquid coupled to a centrifugator that selects only the smallest particles.

The seeding is made downstream of the test section, which allows an efficient mixing of the particles into the returning flow of the wind tunnel. This results in a satisfying homogeneity inside the test section.

Time resolution of the PIV is obtained through phase averaging locked to the airfoil motion. In this process, the period of the airfoil motion is decomposed into N phases, each phase being at a time t_k such that

$$t_k = (k - 1)\frac{1}{N f_g} \quad \text{for} \quad k = 1, \dots, N \tag{11}$$

The phasing system, based on an field-programmable gate array, serves as an external trigger to the PIV laser and camera. An ensemble of M couples of images are recorded in each of the N phases. Here, N was set to 8 and $M = 300$, which represents an ensemble of 2400 images for each run and an acquisition time of approximately 20 min. The choice of M was checked to be enough on the basis of a preliminary convergence study of the PIV data performed over an acquisition of 1000 pairs of images.

The PIV images are treated with a GPU based, in-house software which uses a minimization technique to calculate the vector field instead of the classical correlation technique (see Leclaire et al. 2009). Square windows of 31 pixels are used. The quality of the vector calculation is given by the value of the score S which denotes the performance,

Fig. 10 Angle of the flow in the empty test section without the gust generator. **a** Shows the PIV data at $M = 0.73$ and **b** gives a comparison with the probe data along a vertical line at $x = 1.1$ m. In **b** the data obtained by the PIV and the probe has been artificially set to zero at $z = 0$

(a) PIV field

(b) Comparison between PIV and probe
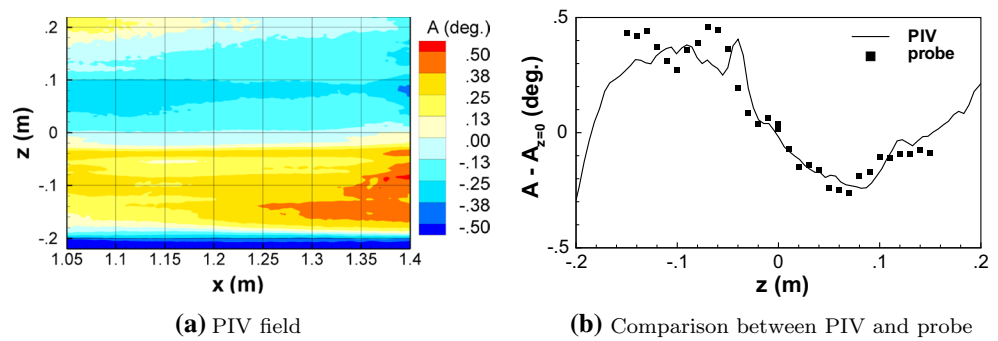
between 0 (bad) and 1 (good), of the minimization process. All the tests carried out feature $S \geq 0.4$, which is well in the range of the usually accepted values. The lowest scores were obtained at transonic speeds, for which seeding the flow becomes challenging, due to limited flow rate of seeding particles provided by the seeding system. It was found that the seeding was ideally suited for the lower speed ($M = 0.3$) but slightly insufficient for the higher speeds, even though it was set to its maximum capacity.

Another difficulty of the present PIV measurements relates to the small displacement of the particle in the vertical direction compared to their longitudinal displacement. For instance, generating gusts with a 1° angle would lead to a ratio $w'/U_0 \simeq 0.02$ (w' is the disturbance vertical velocity). This means that in a given time period, a particle will displace 50 times less in the vertical than in the horizontal direction. Considering the usual displacement of 5 pixels in between two successive snapshots of the flow, this means that one only has 0.1 pixels displacement in the vertical direction. This value of 0.1 pixel is generally the precision attributed to any PIV system. Subpixel precision results from the interpolation schemes of the PIV softwares (in the present case, B-spline interpolation). Therefore, measuring a 1° flow incidence is close to the limit of any PIV system. A solution to this problem was to increase the time between two snapshots so that the pixel displacement was ten times larger than the usual value of 5 pixels. A guess value of the particle displacement was then indicated to the software so that it could correlate the snapshots. This allowed a successful determination of the vertical velocity field. Accordingly, using the 0.1 pixel conservative uncertainty, the horizontal displacement of 50 pixels yields an uncertainty of about 0.2 % on the horizontal component. Concerning the vertical component, considering a flow angle of 1°, the vertical displacement is roughly 0.5 pixels, which causes an uncertainty on the order of 20 %, thus much higher than in the horizontal direction.

The phase-averaged technique provides averaged velocity fields $\boldsymbol{u}_k(x, z; t_k)$ at each kth phase of the N phases that decompose the motion of the oscillating airfoils. Each phase spans the time period $t \in [t_k, t_{k+1}]$ with t_k defined in

(11). Treatment of the data includes subtracting the phase mean defined by

$$\overline{\boldsymbol{u}}(x, z) = \frac{1}{N} \sum_{k=1}^{N} \boldsymbol{u}_k(x, z; t_k) \tag{12}$$

The difference about this mean for the kth phase average is then given by

$$\boldsymbol{u}_k'(x, z; t_k) = \boldsymbol{u}_k(x, z; t_k) - \overline{\boldsymbol{u}}(x, z) \tag{13}$$

In addition, the following space average is defined

$$\langle \boldsymbol{u}_k \rangle (t) = \frac{1}{V} \int_{\mathrm{v}} \boldsymbol{u}_k(x, z, t) \mathrm{d}x \mathrm{d}z \tag{14}$$

The volume V is defined by $1\,\mathrm{m} < x < 1.4\,\mathrm{m}$ and $-0.1\,\mathrm{m} < z < 0.1\,\mathrm{m}$. This volume is introduced in order to estimate the spatial uniformity of the gust in the central part of the test section in between the wakes of the airfoils. This test volume corresponds to the typical location of a wing model in the S3Ch wind tunnel. In particular, the flexible model will be installed there in the future tests mentioned in the introduction. The spatial averaging given by (14) provides a useful estimate of the gust properties seen by the model. The limits of the volume in the horizontal direction generate a rectangular field that corrects the trapezoidal shape of the PIV plane.

2.4 Flow variations in the absence of the generator

The generator modifies the flow in the test section by oscillating it up and down. As such, the knowledge of the uniformity of the flow produced by the wind tunnel without the gust generator is a preliminary step in the analysis of the gusts. Figure 10 shows the vertical velocity field in the central plane obtained by the PIV and the comparison with the probe when the wind tunnel is operated at $M = 0.73$. It can be noticed that the flow inside the tunnel is not strictly uniform. The lower part of the test section exhibits a slightly upward flow component, while the upper part shows a slightly downward component. In addition to this, spatial variations of scale around 0.05 m are observed in

the vertical direction. The comparison with the two-hole pressure probe is remarkable. This conforts the quality of the measurements. Similar comparisons were performed at the other test values of the Mach number, with similar agreement.

3 Dynamic model of the flow

A dynamic model, based on a vortex element discretization of the flow, is introduced to account for the time-dependent flow changes. It allows a finer description compared to the simple model described in Sect. 1.2. In particular, the two airfoils are modeled and their wakes are allowed to evolve freely.

3.1 Vortex element method

In this section, the vortex element theory is shortly recalled. The flow is supposed incompressible, and the compressibility effects are accounted for, like in Sect. 1.2, by the Prandtl–Glauert analogy. Each airfoil is modeled as a segment $[x_l, x_t]$ between the leading and the trailing edges. The model takes into account n_a airfoils with here $n_a = 2$. The two airfoil move synchronously, the evolution of α_g being given by (1). A number $n_a \times N_b$ of bound vortices of individual circulation $\Gamma^b_{i=1,n_aN_b}$ are distributed along the airfoils to model lift. Free vortices of circulation $\Gamma^f_{i=1,N_f}$ are shed into the flow as a consequence of the Kutta condition at the trailing edge. The free and bound vortices are located at the positions $x^f_{i=1,N_f}$ and $x^b_{i=1,n_aN_b}$, respectively, the latter being uniformly distributed along $[x_l, x_t]$. Control points x^c, offset relatively to the bound vortices by a half discretization step of the bound distribution, are introduced to apply the following no-through flow boundary condition at the airfoils

$$\left[U_0 e_x - \frac{dx^c}{dt} + \sum_{i=1}^{n_aN_b} u_{ij}(\Gamma^b_i) + \sum_{i=1}^{N_f} u_{ij}(\Gamma^f_i) \right] \times n_j = 0 \quad (15)$$

The solution of (15) determines the bound vorticity. The first term in (15) is the inflow velocity. The second term is the velocity induced by the motion of the airfoil. Simple dimensioning of the terms shows that this term can be neglected if $St << 1$. The third term is the velocity induced at the control points by the bound vortices. Finally, the fourth term is the velocity induced at the control points by the free vortices. The velocity u_{ij} is the velocity induced by a point vortex located at x_i at a point x_j. The direction perpendicular to the airfoil is $n_j = \sin \alpha_g e_x + \cos \alpha_g e_z$. The free vortices are lagrangian elements that move according to the induction by all the other vortices. At every time step, the new location of the free vortices is obtained by summing all these contributions. The time derivative is

carried out using a first-order time scheme and thus the vortex position at time $t^m = t^{m-1} + \Delta t$ is given by

$$\frac{x^f_k(t^m) - x^f_k(t^{m-1})}{\Delta t} = \sum_{i=1}^{n_aN_b} u_{ik}(\Gamma^b_i) + \sum_{i=1|i\neq k}^{N_f} u_{jk}(\Gamma^f_j) \quad (16)$$

In addition to the no-through flow boundary condition, a second condition, the conservation of the total circulation, applies. Let the initial circulation in the flow be Γ_0 then the following relation holds

$$\sum_{i=1}^{n_aN_b} \Gamma^b_i + \sum_{i=1}^{N_f} \Gamma^f_i = \Gamma_0 \quad (17)$$

Using conditions (15) and (17), one can form the following linear system whose solution gives the values of the bound circulation vector $X = \left(\Gamma^b_1 \; \Gamma^b_2 \; \cdots \; \Gamma^b_{n_aN_b} \right)^T$

$$AX = f \quad (18)$$

with A a square matrix of size n_aN_b defined by

$$A_{ij} = \begin{cases} u_{ij}(1) \times n_j & \text{if} \quad j \neq (1,\ldots,n_a)N_b \\ 1 & \text{if} \quad j = (1,\ldots,n_a)N_b \end{cases} \quad (19)$$

and f the right-hand side of size n_aN_b

$$f = \begin{pmatrix} -\left(U_0 e_x + \sum_{k=1}^{N_f} u_{ij}\left(\Gamma^f_i\right) \right) \times n_j \\ \Gamma_0 - \sum_{i=1}^{N_f} \Gamma^f_i \end{pmatrix} \quad (20)$$

At initial time, no free vortex is present in the flow. As the airfoils begin to oscillate, the change in circulation is compensated by the shedding of free vortices at the trailing edges. Since the Kutta condition requires that $\Gamma^b_{(1,\ldots,n_a)N_b} = 0$ this condition is enforced by transferring the circulation $\Gamma^b_{(1,\ldots,n_a)N_b}$ at the trailing edge obtained after solving (18) to the new free vortices, which are introduced at the locations

$$x^f_{N_f+1,\ldots,n_a} = x_{t,1,\ldots,n_a} + U_0 \frac{\Delta t}{2} \begin{pmatrix} \cos \alpha_g \\ -\sin \alpha_g \end{pmatrix} \quad (21)$$

where a particle leaving the trailing edge would be after half a time step, when traveling at a velocity U_0 from the trailing edge. The number N_f is incremented $N_f \rightarrow N_f + n_a$ following the introduction of the new free vortices.

The effect of the walls is modeled by infinite arrays of vortices in association to each vortex present in the model, bound and free. This is accomplished by using formulae (8) for the velocity field induced by each vortex. The use of image vortices allows to comply with the no-through flow at the walls. In this model, the walls are supposed straight. In particular, the curvature of the nozzle part of the setting where the airfoils are placed experimentally is not modeled.

(a) w'/U_0

(b) u'/U_0
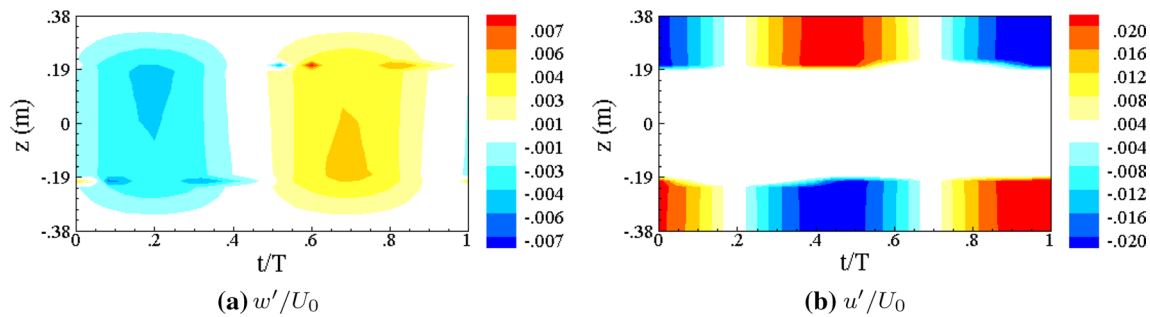
Fig. 11 Perturbation velocity field for case 6: $M = 0.73$ and $f_g = 40\,\text{Hz}$, as a function of time, at $x = 1.2\,\text{m}$. **a** is w'/U_0 and **b** is u'/U_0

Fig. 12 Comparison of the wake obtained by the numerical model and that measured by PIV in case 6, $M = 0.73$ and $f_g = 40\,\text{Hz}$. The time sequence runs over the times $t_{1,3,5,7}$ of the phase averages. The wake vorticity of the dynamic model appears in *red discs* and the PIV is the field of $< u'w' >$ in *gray scale*
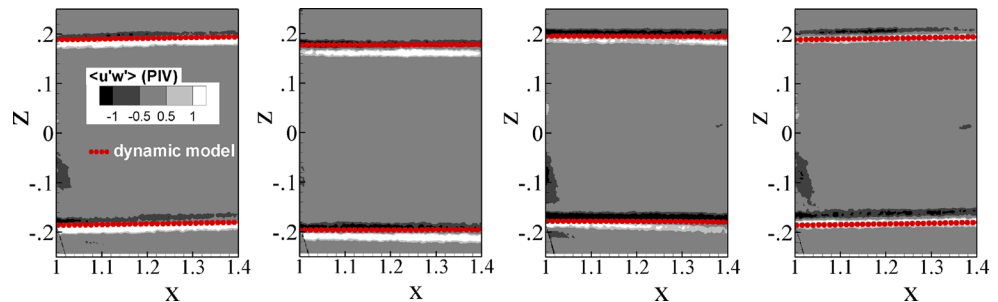
Finally, using this flow model, any velocity vector can be determined by summing the contributions from all the vortices present in the flow. Note that, for a given geometry of the setting, the flow thus obtained is fully determined by the Strouhal number.

$$\boldsymbol{u}(\boldsymbol{x}) = \sum_{i=1}^{n_a N_b} \boldsymbol{u}_i\left(\Gamma_i^b\right) + \sum_{i=1}^{N_f} \boldsymbol{u}_i\left(\Gamma_i^f\right) \qquad (22)$$

3.2 Flow topology

The flow field inside the channel features a complex pattern that can be best observed by considering the temporal evolution of the vertical velocity profile taken at a given longitudinal location x. This means looking at $\boldsymbol{u}(\boldsymbol{x}, t)$ for a prescribed x as a function of time over one period $T_g = f_g^{-1}$ of the airfoils motion. The temporal evolution of the profile taken at $x = 1.2\,\text{m}$ is shown in Fig. 11. Figure 11a shows the vertical velocity field. It comprises close to homogeneous zones of alternatively upward and downward velocity in between the walls. The vertical flow goes to zero at the wall as expected due to the slip condition imposed by the images vortices. The wakes of the airfoils deteriorate the homogeneity of the flow at $z = \pm 0.2\,\text{m}$, thus reducing the usable part (from the point of view of the future tests with the flexible model) of the test section to a zone in between these wakes.

As for the horizontal velocity field shown in Fig. 11b, one sees that only small fluctuations of the wind tunnel velocity are present inside the central part of the flow stream whereas strong longitudinal velocities are observed close to the walls. This results from the proximity of the vortices of opposite sign in the pair formed by the primary wake vortices and their images about the walls. The magnitude of the perturbation longitudinal velocity reaches 2 % of the upstream flow speed close to the walls, but it is only on the order of 0.1 % in the central part of the flow.

Figure 12 shows the comparison between the location and form of the wake predicted by the numerical model and that obtained with the PIV measurement in case 6 ($M = 0.73$, $f_g = 80\,\text{Hz}$). This plot provides a qualitative validation of the numerical tool. The $< u'w' >$ Reynolds stress is used to highlight the wake in the PIV data. This quantity was found to be the most indicative of the wakes, certainly because of the strong shear present in this region. The numerical wake is synchronized to the experimental data at the first time step and then taken at the times of the phase averages $t_{k=1,8}$. It is found that the numerical prediction is in good agreement with the experimental data. This comparison led us to slightly modify the vertical position h_g of the airfoils in the numerical model to increase the agreement with the PIV data. Taking the height of the airfoils at $h_g = 0.2\,\text{m}$ like in the experimental setting resulted in a shift of about 0.01 m in the position of the wake predicted by the model compared to the experiment. Therefore, the height of the airfoil in the model was adjusted to $h_g = 0.19\,\text{m}$.

Fig. 13 Vertical velocity fields w'/U_0 for the eight phase averages obtained by PIV in case 6, $M = 0.73$ and $f_g = 80\,\text{Hz}$
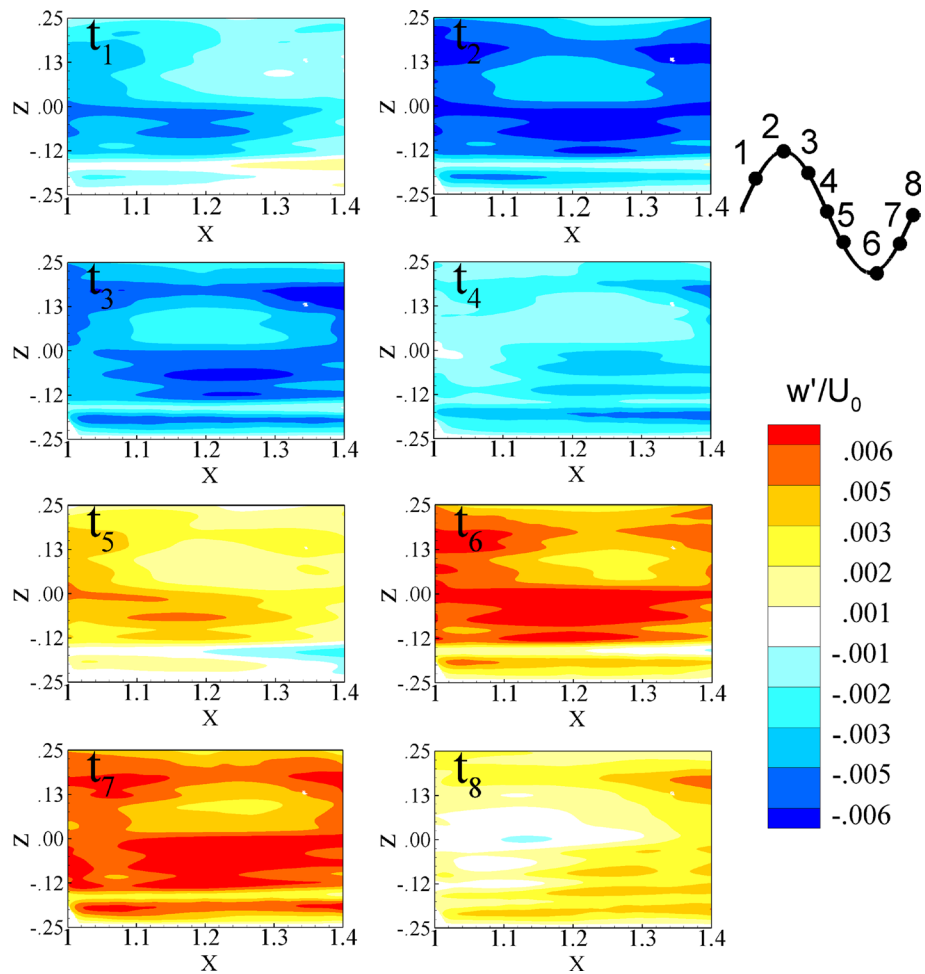
4 Results

4.1 PIV results

The vertical velocity field obtained with the phase-averaged PIV in case 6, characterized by $M = 0.73$ and $f_g = 80\,\text{Hz}$, is shown in Fig. 13. The average flow field $\overline{\boldsymbol{u}}$ has been subtracted from the total flow field to yield the perturbation $\boldsymbol{u}'$ at each of the eight phase averages recorded by the PIV system. The oscillations of the flow is well apparent when going through these snapshots. However, the uniformity of the gust is disturbed by vertical variations of the flow field, in the form of longitudinal streaks. The same pattern was observed with the pressure probe, when looking at the flow component at the generator frequency, hence excluding any measurement errors by the PIV. Several tests have also been carried out in order to analyze the influence of the generator frequency and of the Mach number. While changes in amplitude were found, the pattern remained. Taking into account the similarity with the flow variations observed in the case without the gust generator in Fig. 10, it is likely that

the gusts are disturbed by the nonuniformity of the flow generated by the wind tunnel. These disturbances are of the same order of magnitude as those produced by the gust generator, thus significantly impacting the resulting flow.

In the following, the flow is averaged in order to lessen the impact of these disturbances and highlight the structure of the gusts. To do so vertical profiles at several longitudinal positions are considered and then resliced over one period of the airfoil oscillation. The different slices are then averaged. In this process, the vertical profile at a position x_j is first transformed following

$$\boldsymbol{u}'_k(x_j, z) = \hat{\boldsymbol{u}}(\tau_{kj}, z) \tag{23}$$
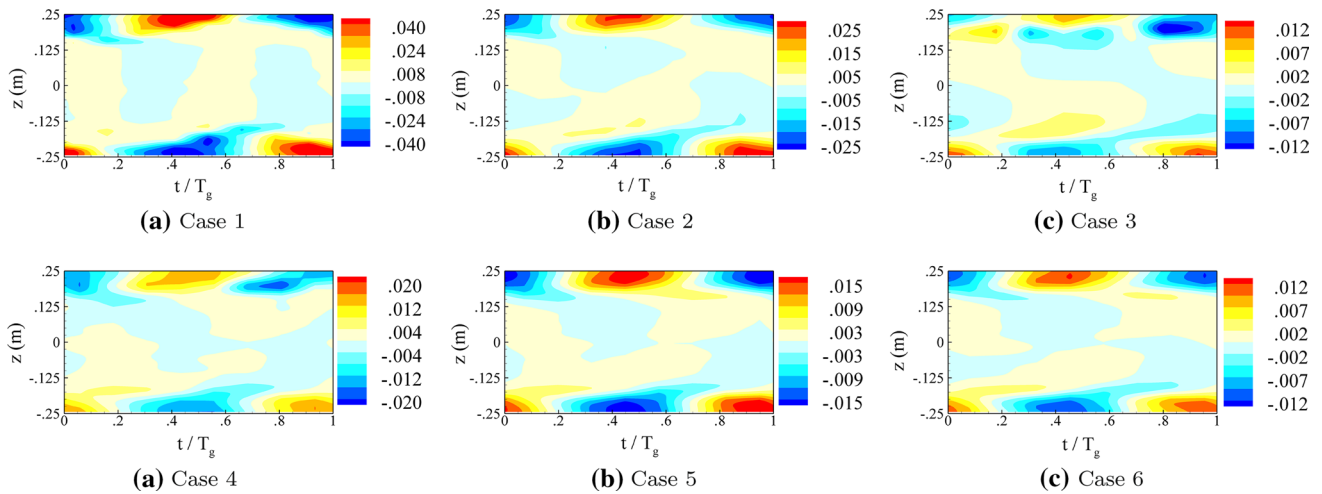
with

$$\tau_{kj} = t_k - \frac{x_j}{U_0} \tag{24}$$

and $j = 1, \ldots, N_s$ where N_s is the number of vertical profiles that are considered. Relation (24) accounts for the transport of the gust at the inflow velocity U_0. The average over the N_s profiles is then obtained as follows
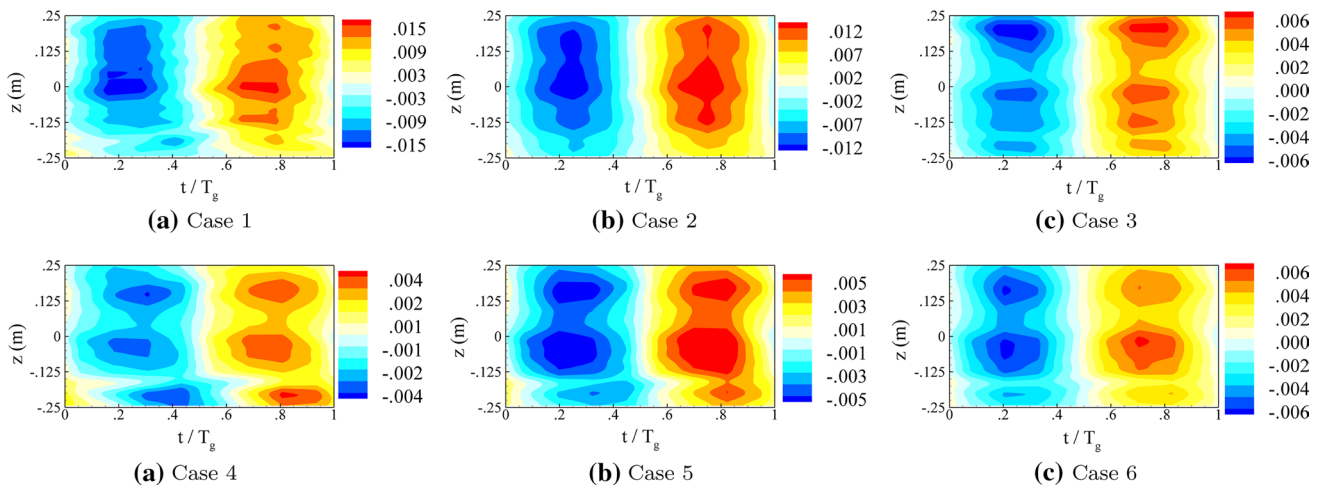
Fig. 14 Normalized vertical velocity field $\tilde{w}/U_0$ for the PIV cases 1–6 (see Table 1)

Fig. 15 Normalized horizontal velocity $\tilde{u}/U_0$ for the PIV cases 1–6 (see Table 1)

$$\tilde{u}(\tau_k, z) = \frac{1}{N_s} \sum_{j=1}^{N_s} \hat{u}(\tau_{kj}, z) \qquad (25)$$

where τ_k spans one period of the airfoil oscillations $T_g = f_g^{-1}$.

Figure 14 shows the resulting flow fields, in a manner identical to Fig. 11. These flow fields have been averaged over $N_s = 20$ longitudinal locations. Each frame shows the flow variations over one wavelength of the gust. Apart from the previously observed small-scale disturbance pattern, the gusts exhibit particularly well-balanced up and down drafts that occupy half of the wavelength each. The associated waveform features a qualitatively sinusoidal pattern, with a vertical wavefront.

Figure 15 shows the longitudinal velocity fields. The flow topology is identical to the one given by the dynamic model. The longitudinal component of the flow is little perturbed (less than 0.1 % of the inflow velocity) in the middle of the test section, while the walls induce high velocities close to them (above and below the upper and lower wakes, respectively).

4.2 Gust uniformity

The gust uniformity in the test volume V is further analyzed by estimating the spatial average of the vertical velocity and the standard deviation through relation (14). The PIV, probe and dynamic model are compared altogether in Fig. 16 for a selection of the PIV test cases (see Table 1). The experimental data is normalized on A_g and β, according to the earlier analytical developments. The probe data correspond to the sinusoidal variation with the amplitude at the frequency f_g of the oscillating airfoils. The vertical bars

Fig. 16 Comparison between PIV, probe and dynamic model in terms of the normalized gust amplitude, as a function of time normalized on the period T_g of the oscillation. The *vertical bars* indicate the standard deviation of the PIV data in the test volume V. The PIV data are fitted by a spline curve. **a** Corresponds to the PIV case 1, **b** to case 3, **c** to case 4 and **d** to case 6

(a) $St = 0.038$, $M = 0.3$

(b) $St = 0.15$, $M = 0.3$

(c) $St = 0.016$, $M = 0.73$

(d) $St = 0.065$, $M = 0.73$
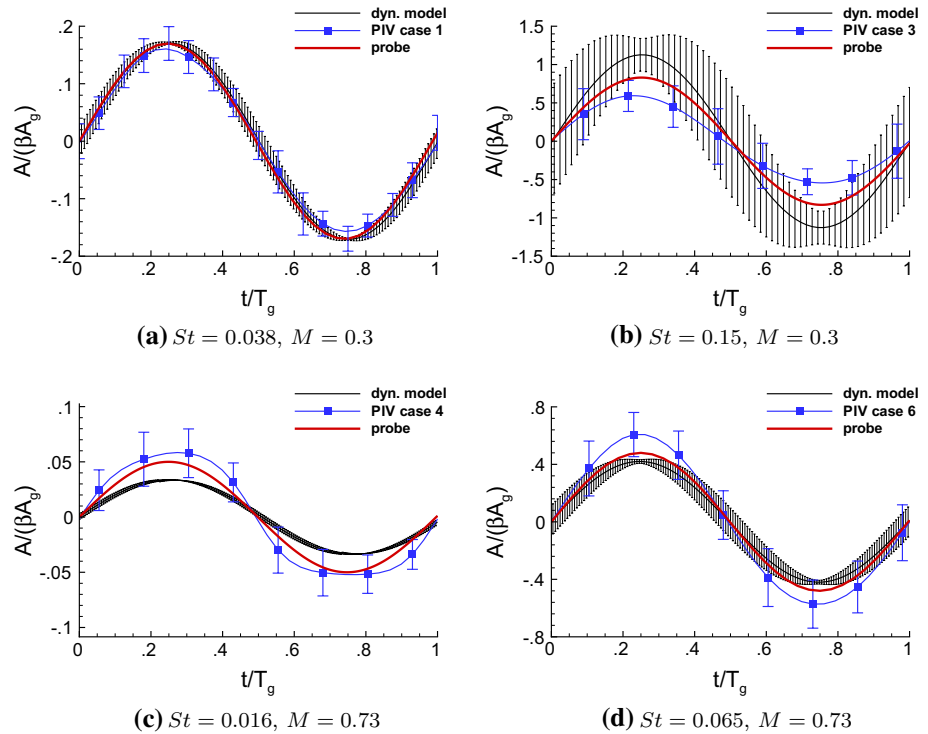
attached to the PIV points indicate the standard deviation of the vertical velocity field in V. There is a close agreement between the PIV, the probe and the dynamic model. The largest difference between the model and the experiment is observed at $St = 0.15$, certainly because in this case, the gust-induced angle are small, and more sensible to the natural disturbances of the wind tunnel flow. Moreover, the PIV data are consistently marked by an important value of the spatial deviation about the averaged signal, whatever the Strouhal and Mach numbers. Here, also the disturbances due to the wind tunnel flow likely contribute to a large part of these deviations.

Figure 16 shows that the waveform of the gust is close to sinusoidal in all the test cases. In this context, Fourier analysis of the PIV data, which has been carried in the course of this study, provides no improvement in the analysis compared to the phase averages and the treatments of Fig. 16 and therefore is not detailed here.

It is interesting to note that the dynamic model indicates that the standard deviation increases with the Strouhal number. The origin of this increase can be understood by looking at the changes in the wake when the Strouhal number is increased. Figure 17 draws the wakes behind the oscillating airfoils for a selection of frequencies. It clearly shows that the wake deformations induced by the airfoil motion and by the self-instability of the vortex sheets attain stronger amplitudes when the frequency is increased. At the lowest frequency shown ($St = 0.04$) the wake is almost straight, alike the simple model that was introduced at the beginning
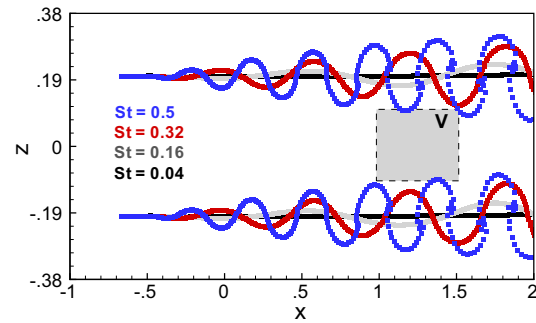

Fig. 17 Snapshot of the wake obtained with the dynamic model, for several Strouhal numbers. The test volume V where the evaluation of the gust is performed is indicated

of the article, as soon as $St = 0.15$ the wake deformations become qualitatively sensible inside the test volume V. The largest frequency displayed, $St = 0.5$ leads to massive deformations that directly interfere with the volume V.

4.3 General performances

The amplitude of gust obtained in all the experimental test performed (probe and PIV) are summarized in Fig. 18. The results of the dynamic model, with and without the walls, are indicated for comparison. The three sets of data are in close agreement over the frequency range of the tests ($St \in [0.016, 0.15]$). When the walls are removed, the incidence ratio is strongly overestimated.

Fig. 18 Performance of the gust, experimental and numerical data. **b** is a zoom in the low Strouhal range of frame (**a**). The experimental data are recast into its incompressible form through the Prandtl Glauert similarity, i.e.. by dividing the raw results by $\beta = (1 - M^2)^{-1/2}$
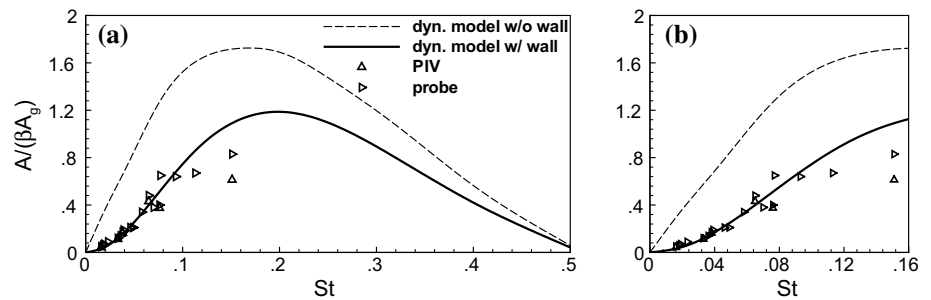
Interestingly the dynamic model shows that the gust amplitude evolves following a three-stage behavior when the frequency is increased, with a positive slope in the low Strouhal range, a plateau when $St \in [0.15, 0.25]$ and a decrease when $St > 0.25$. Notably enough, this decrease, which was not predicted by the analytical model (7), makes it almost impossible to generate vertical gusts when the frequency is too high, since at $St = 0.5$ the gust amplitude is almost canceled. An explanation is provided by Fig. 17 which shows that the reduction in the vertical velocities is correlated to the deformations of the wakes. In fact, when the wake deforms, the induction velocity by the wake vortices tends to interfere negatively, still leading to flow variations, but those are not ordered in the form of a clear vertical gust anymore. Such deformations of the wakes are a clear limitation of the present methodology to generate gusts, which is based on the idea that the varying up and down drafts generated by the oscillating airfoils are transported downstream with minor changes. In fact the self-instability of the vortex sheet, here promoted by the oscillating generators, provokes a deterioration of this transport in the high frequencies, thereby limiting the working range of the present apparatus.

In this range, the present apparatus works well though, providing incidence ratios A/A_g of up to 0.4 at transonic speeds, the maximum being $A/A_g \simeq 0.9$, at $M = 0.3$ and $sf_g = 80$ Hz. It is interesting, for comparison purposes, to look at the performances of similar devices described in the literature. Mirick et al. (1990) reports incidence ratio of up to 1.3 in the Langley Transonic tunnel operated at low speed. Unlike the present findings, the increase in gust frequency in Mirick's tests leads to a reduction in the gust amplitude. This probably results from the use of longitudinal trailing vortices as the mechanism to generate the gusts. With an increase in frequency, trailing vortices occupy the same position but their intensity is reduced due to the roll-up time of the longitudinal vortices being relatively longer compared to the advection time. With a spanwise apparatus similar to the current one but comprising a column of six airfoils, Buell (1969) generated ratios on the order of 1.5 at speeds up to 80 m/s in a range of Strouhal number identical to the present study. In

particular, Buell also finds that the gust amplitude increases with the Strouhal number. Tang et al. (1996), with a system that combines airfoils and rotating slotted cylinders behind each airfoil to oscillate the lift, obtain ratio up to 1 at low speeds in a range of Strouhal between 0 and 0.08, but observe a decrease in this ratio with the Strouhal number. Grissom and Devenport (2004), with a multiple pitching airfoil, obtain ratio of 0.9 at speeds 15 m/s and find a beneficial effect of the Strouhal number.

5 Conclusion

A new gust generator device has been tested at sub and transonic speeds at ONERA S3Ch wind tunnel. The gust generator consists in a pair of airfoils oscillating at frequencies up to 80 Hz for incoming flow speed ranging from Mach 0.3 to 0.73, corresponding to a maximum Strouhal number of 0.15. First a theoretical approach to the problem has been introduced in order to reveal the scaling parameters of the gust device, namely the Strouhal and Mach numbers and the oscillation amplitude of the airfoils. The model also allowed to evaluate the effect of the walls of the test section on the gust. Those significantly reduce the gust amplitude, all the more so as the wavelength of the gust is large, thereby affecting the low Strouhal gusts of the present experiments. In contrast, the Strouhal and Mach number and the oscillation amplitude have a beneficial effect on the gust amplitude, at least when the Strouhal is kept smaller than 0.2. This latter limitation could be obtained by using a dynamic model of the flow. This model, which represents the main feature of the experiment through an inviscid approach, has been established to provide predictive capabilities on the gust shape and amplitude at a low computational cost. The close agreement between the experimental data and the dynamic model shows that the flow downstream of the oscillating airfoils is mostly governed by the dynamics of the vorticity associated with the wakes. In the low range of Strouhal number investigated here and due to the rather close proximity between the test volume and the generator devices, the wakes exhibit little deformation and suffer negligible diffusion. This explains (1) the

good agreement with the inviscid model, (2) the pure harmonic waveform of the gusts and (3) the satisfying spatial uniformity. The latter was found to be mainly impacted by the natural flow disturbances produced by the wind tunnel. These generate small-scale variations that modify locally the amplitude of the gust but do not change its global shape. Adequate post-processing of the data showed that the gust were globally uniform and sinusoidal. At transonic speeds, the maximum flow angle is about 0.3°, representing vertical velocities of about 1.2 m/s.

The oscillating airfoil strategy appears as an efficient solution to generate gusts at subsonic speeds in the range of low Strouhal numbers. The next step in the experimental program, with the flexible model in test section, proved that the gust generated by this system are sufficient to induce aeroelastic effects. While this setting has only been used to generate vertical gusts, it could also be used to generate streamwise gusts or combinations of the two. In a recent experimental work at low speed, Harding and Bryden (2012) show that it is possible to design gust as desired by inverting a flow model such as the one used in the present study. This opens interesting possibilities for any future use of the present device.

References

Bennett R, Gilman J Jr (1966) J Aircr 3(6):535

Borland C, Schindel L (1967) Supersonic gust simulation experiments. AIAA J 5(10):1910

Brunele E, Consigny H (1989) 72nd semi annual meeting, Princeton University

Buell D (1969) An experimental investigation of the velocity fluctuations behind oscillating vanes. Technical Report NASA TN D-5543

Clementson G (1950) An investigation of the power spectral density of atmospheric turbulence. Ph.D. thesis, Massachusetts Institute of Technology

European Aviation Safety Agency (2013) Acceptable means of compliance for large aeroplanes cs-25. Technical Report

Grissom D, Devenport W (2004) Developement and testing of a deterministic disturbance generator. 10th AIAA/CEAS Aeroacoustics Conference. doi:10.2514/6.2004-2956

Harding S, Bryden I (2012) J Fluid Mech 713:150

Huvelin F, Girodroux-Lavigne P, Blondeau C (2013) Forum on aeroelasticity and structural dynamics. Bristol, UK

Kobayakawa M, Maeda H (1978) J Aircr 15(8):540

Krause S (2003) Aircraft safety: accident investigations, analyses, and applications. McGraw-Hill, New York

Lamb H (1993) Hydrodynamics. Cambridge University Press, Cambridge

Leclaire B, Jaubert B, Champagnat F, Le Besnerais G, Le Sant Y (2009) Proceedings of 8th International Symposium on Particle Image Velocimetry-PIV09, Melbourne

Levine J, Garstand M, Laseur NE (1973) A measurement of the velocity field of a cumulus cloud. J Appl Meteorol 12:841–846

Liauzun C (2010) ASME 2010 3rd Joint US-European Fluids Engineering Summer Meeting collocated with 8th International Conference on Nanochannels, Microchannels, and Minichannels (American Society of Mechanical Engineers), pp. 269–276

Mai H, Neumann J, Hennings H (2011) Gust response: a validation experiment and preliminary numerical simulations. In: International Forum onAeroelasticity and Structural Dynamics (IFASD), Paris

Mirick P, Hamouda MNH, Yeager Jr W (1990) Wind tunnel survey of an oscillating flow field for application to model helicopter rotortesting. Technical Report NASA TM 4224/AVSCOM TR 90-B-007

Reginald B, Bland B, Reisert T (1947) An application of statistical data in the development of gust load criterions. Techical Report, NASA TN 1268

Reid C, Wrestler Jr C (1961) An investigation of a device to oscillate a wind tunnel airstream. Technical Report NASA-TN-D-739

Ricci S, Scotti A (2008) 49th AIAA/ASME/ASCE/AHS/ASC structures, structural dynamics, and materials conference

Tang D, Cizmas PG, Dowell E (1996) J Aircr 33(1):139

Theodorsen T (1992) This paper is also included in a modern view of Theodore Theodorsen. AIAA, Reston, pp 2–21